Systematic generation of the cascade of anomalous dynamical first- and higher-order modes in Floquet topological insulators

Arnob Kumar Ghosh [1,2,*] Tanay Nag,[3,†] and Arijit Saha [1,2,‡]
[1]*Institute of Physics, Sachivalaya Marg, Bhubaneswar-751005, India*
[2]*Homi Bhabha National Institute, Training School Complex, Anushakti Nagar, Mumbai 400094, India*
[3]*Institut für Theorie der Statistischen Physik, RWTH Aachen University, 52056 Aachen, Germany*

(Received 19 November 2021; accepted 1 March 2022; published 16 March 2022)

After extensive investigation of the Floquet second-order topological insulator (FSOTI) in two dimensions, here we propose two driving schemes to systematically engineer the hierarchy of the Floquet first-order topological insulator, the FSOTI, and the Floquet third-order topological insulator in three dimensions. Our driving protocols allow these Floquet phases to showcase regular 0, anomalous π, and hybrid 0-π-modes in a unified phase diagram, obtained for both two- and three-dimensional (2D and 3D) systems, while starting from the lower-order topological or nontopological phases. Both the step drive and the mass kick protocols exhibit the analogous structure of the evolution operator around the high symmetry points. These eventually enable us to understand the Floquet phase diagrams analytically and the Floquet higher-order modes numerically based on finite-size systems. The number of 0 and π modes can be tuned irrespective of the frequency in the step drive scheme, while we observe frequency-driven topological phase transitions for the mass kick protocol. We topologically characterize some of these higher-order Floquet phases (harboring either 0 or anomalous π mode) by a suitable topological invariant in 2D and 3D cases.

DOI: 10.1103/PhysRevB.105.115418

I. INTRODUCTION

With the discovery of the quantum Hall effect [1], topological electronic materials have gained an immense amount of attention for their gapless boundary modes as caused by the nontrivial winding of the ground-state wave function of gapped bulk systems [2]. Instead of applying an external magnetic field, the quantum anomalous Hall effect opens up a new avenue of research to be explored in the future [3]. The introduction of spin-orbit coupling further enriches the research activity in this field when time-reversal symmetry (TRS) preserves the quantum spin Hall insulator [4–6], thus giving rise to the famous idea of a topological insulator (TI) [7–9]. Consequently, the concept of a TI has been contextualized in several real materials [10–12], paving the way for the realization of bulk-boundary correspondence where gapless boundary modes are the outcome of the topological band structure of bulk crystal. These can be exemplified for the first-order TI. Very recently, the concept of higher-order topological insulators (HOTIs) [13–25] received an enormous amount of attention in modern quantum condensed-matter research. The bulk-boundary correspondence is generalized such that a d-dimensional nth-order HOTI is portrayed by the emergence of $(d-n)$-dimensional boundary modes. In particular, a two-dimensional (three-dimensional) [2D (3D)] second-order topological insulator (SOTI) hosts zero-dimensional (one-dimensional) [0D (1D)] corner (hinge) modes, whereas a 3D third-order topological insulator (TOTI) hosts 0D corner modes.

Moving our attention to systems out of equilibrium, we emphasize that periodically driven quantum systems [26,27] exhibit intriguing properties as compared to their static counterparts, such as dynamical localization [28–30], many-body localization [31–33], Floquet time crystals [34,35], higher harmonic generation [36,37], etc. Intriguingly, nondissipative dynamical boundary modes, due to their time translational symmetry, can be contrived in a Floquet topological insulator [38–43] and a Floquet topological superconductor [44–47], which have recently been the prime focus of interest. The nontrivial winding of the wave function for these driven systems in the time direction further allows one to have anomalous boundary modes, namely π modes, at finite energy. The prodigious experimental development of Floquet systems based on a solid-state setup [48], acoustic systems [49,50], photonic platforms [51,52], etc., adds further merit to this field with regard to their realization and possible device application. Interestingly, Floquet engineering also enables one to achieve Floquet HOTI (FHOTI) and HOT superconductor phases starting from a lower-order or nontopological phase by suitably tuning appropriate driving protocols [53–68].

Given the above background on static and driven topological systems, we would like to emphasize that the systematic generation of anomalous HOTI phases (anchoring both regular 0 and anomalous π mode), in both 2D and 3D, has not been explored so far to the best of our knowledge, although a few attempts have been made by activating the tight-binding piecewise in a steplike manner to show the emergence of

*arnob@iopb.res.in
†tnag@physik.rwth-aachen.de
‡arijit@iopb.res.in

anomalous π corner modes in two dimensions [57,63,64]. We note that the FHOTI states are not necessarily formulated from the underlying lower-order topological state. On the other hand, very recently regular static zero-energy corner and gapless hinge modes have been shown in a hierarchical manner starting from the lower-order topological states [53,61,69]. Therefore, merging the above two aspects together, an immediate question arises regarding how to generate the flow of anomalous first-order topological insulator (FOTI) and HOTI phases starting from a trivial or static topological phase in both two and three dimensions. We refer to these phases as Floquet FOTI (FFOTI), Floquet SOTI (FSOTI), and Floquet TOTI (FTOTI).

In this article, we consider a steplike driving scheme, incorporating appropriate Wilson-Dirac mass terms in a simple tight-binding model to explore the appearance of the dynamical FFOTI as well as all the FHOTI phases in two and three dimensions. Interestingly, we find that the FFOTI phase diagrams, hosting 0, π, 0-π edge (surface) modes (see Figs. 1 and 3), are directly upgraded into FSOTI (FSOTI and FTOTI) phase diagrams in 2D (3D) conceiving 0, π, 0-π corner (hinge and corner) modes as shown in Fig. 2 (Figs. 4 and 5). Without restricting ourselves to the above particular driving scheme, we also exemplify the identical findings by considering a mass kick protocol (see Fig. 6), where we find frequency-driven topological phase transitions in addition to the parameter-driven phase transitions. We analytically analyze the possible reason behind such systematic formulation of the FFOTI and the FHOTI phases from the Floquet operator that can signal the nonequilibrium phase diagram unanimously. We characterize some of these phases by an appropriate topological invariant, such as tangential polarization and octupolar moments (see Fig. 7). Furthermore, we illustrate the mosaic phase diagram, consisting of phases with different numbers of 0 and π modes, as a function of parameters associated with the driving (see Fig. 8). We discuss several ancillary aspects of our analysis, such as the high-frequency limit, the consequences of laser driving, the effect of disorder etc., to highlight the importance of our findings. We believe that our work is experimentally viable due to the recent advancements in solid-state materials [70,71], mechanics [72], acoustics [73], microwaves [74], photonics [75], electrical circuits [76], etc.

The remainder of the paper is structured as follows. In Sec. II, we introduce our two types of driving protocols along with the model Hamiltonians. Section III is devoted to a discussion of the main results of the paper, where we present the anomalous dynamical modes both in two and three dimensions for the FFOTI and the FHOTIs. In Sec. IV, we discuss the topological characterization of the FHOTI phases. After that, we discuss other possible approaches to engineer HOTI phases and their stabilization against disorder and a few related aspects in Sec. V. We finally summarize and conclude our paper in Sec. VI.

II. DRIVING PROTOCOLS

Here we enlist our driving protocols in the form of step drive and periodic mass kick for both two and three dimensions.

A. Step drive

The step drive consists of two Hamiltonians that one can employ piecewise within the time period to generate the FFOTI and the FHOTI phases. The driving scheme is explicitly demonstrated below,

$$\begin{aligned} H_{d\mathrm{D}} &= J_1' h_{1,d\mathrm{D}}(\mathbf{k}), \quad t \in \left[0, \frac{T}{2}\right], \\ &= J_2' h_{2,d\mathrm{D}}(\mathbf{k}), \quad t \in \left(\frac{T}{2}, T\right], \end{aligned} \tag{1}$$

where J_1' and J_2' carry the dimension of energy. We work with the natural unit, which allows us to set $\hbar = c = 1$. The drive, however, is controlled by the dimensionless parameters $(J_1, J_2) = (J_1'T, J_2'T)$, where T is the period of the drive. This is related to the driving frequency Ω as $T = 2\pi/\Omega$. Here, $J_i' h_{i,d\mathrm{D}}(\mathbf{k})$ represents the Hamiltonian of the system at the ith step in d-dimension. In particular, to generate a 2D topological phase [53], we consider $h_{1,2\mathrm{D}}(\mathbf{k}) = \sigma_z$ and $h_{2,2\mathrm{D}}(\mathbf{k}) = (\cos k_x + \cos k_y)\sigma_z + \sin k_x \sigma_x s_z + \sin k_y \sigma_y + \alpha(\cos k_x - \cos k_y)\sigma_x s_x$, whereas in three dimensions [61] we envisage $h_{1,3\mathrm{D}}(\mathbf{k}) = \mu_x \sigma_z$ and $h_{2,3\mathrm{D}}(\mathbf{k}) = (\cos k_x + \cos k_y + \cos k_z)\mu_x \sigma_z + \sin k_x \mu_x \sigma_x s_x + \sin k_y \mu_x \sigma_x s_y + \sin k_z \mu_x \sigma_x s_z + \alpha(\cos k_x - \cos k_y)\mu_x \sigma_y + \beta(2\cos k_z - \cos k_x - \cos k_y)\mu_z$. Here, α and β are dimensionless parameters, which we tune to generate the cascade of FFOTI, FSOTI, and FTOTI phases. The three Pauli matrices $\boldsymbol{\mu}$, $\boldsymbol{\sigma}$, and $\boldsymbol{s}$ act on sublattice (A, B), orbital (a, b), and spin $(\uparrow, \downarrow)$ degrees of freedom, respectively.

Note that the first (second) step Hamiltonian $J_1' h_{1,d\mathrm{D}}(\mathbf{k})$ $[J_2' h_{2,d\mathrm{D}}(\mathbf{k})]$ is composed of on-site (hopping) terms only. We sometimes refer to $h_{1,d\mathrm{D}}(\mathbf{k})$ as $h_{1,d\mathrm{D}}$ due to its on-site nature. The α and β independent cosine terms $\cos k_{x,y,z}$ arise due to the nearest-neighbor hopping while the spin-orbit coupling is represented by the sine terms $\sin k_{x,y,z}$. The on-site mass term of strength J_1' becomes very important for the topological phase transition that we discuss below. The first step Hamiltonian thus preserves the necessary symmetries, while the second step Hamiltonian is found to be responsible for breaking certain symmetries. The latter becomes very useful to achieve the FHOTI phases. For $\alpha = \beta = 0$, $h_{i,d\mathrm{D}}(\mathbf{k})$ respects TRS generated by $\mathcal{T} = is_y\mathcal{K}$, where $\mathcal{K}$ is the complex-conjugation operator. However, when $\alpha \neq 0$, which is the corresponding term, $h_{2,d\mathrm{D}}(\mathbf{k})$ breaks both TRS and fourfold rotation (C_4) symmetry while preserving the combined $C_4\mathcal{T}$ symmetry. Importantly, $h_{i,d\mathrm{D}}(\mathbf{k})$ respects unitary chiral $\mathcal{C} = \sigma_x s_y$ $(= \mu_y \sigma_0 s_0)$ and antiunitary particle-hole symmetry $\mathcal{P} = \sigma_x s_z \mathcal{K}$ $(= \mu_x \sigma_y s_y \mathcal{K})$ for two (three) dimensions such that $\mathcal{C} h_{i,d\mathrm{D}}(\mathbf{k}) \mathcal{C}^{-1} = -h_{i,d\mathrm{D}}(\mathbf{k})$ and $\mathcal{P} h_{i,d\mathrm{D}}(\mathbf{k}) \mathcal{P}^{-1} = -h_{i,d\mathrm{D}}(-\mathbf{k})$ [53,61]. It should be noted that the term associated with α further breaks the mirror symmetry.

Before translating to the dynamical limit, we would like to point out the various static phases accessible to our model, depending upon the values of different parameters of the system. One can contemplate the following Hamiltonians in two and three dimensions as

$$H_{2\mathrm{D}}^{\mathrm{Static}}(\mathbf{k}) = J_1' h_{1,2\mathrm{D}}(\mathbf{k}) + J_2' h_{2,2\mathrm{D}}(\mathbf{k}), \tag{2}$$

$$H_{3\mathrm{D}}^{\mathrm{Static}}(\mathbf{k}) = J_1' h_{1,3\mathrm{D}}(\mathbf{k}) + J_2' h_{2,3\mathrm{D}}(\mathbf{k}), \tag{3}$$

where $H_{2D}^{\text{Static}}(\mathbf{k})$ represents the Hamiltonian of a 2D quantum spin Hall insulator (QSHI) with propagating 1D helical edge states, when $\alpha = 0$ and $0 < |J_1'| < 2|J_2'|$ [7,10]. However, for any nonzero value of α, the edge states of the QSHI are gapped out by the corresponding Wilson-Dirac mass term proportional to α in such a way that two consecutive edges incorporate opposite mass terms. Using the generalized Jackiw-Rebbi index theorem [77], one can show the emergence of zero modes at the corners of the system, i.e., the system resides in the SOTI phase [17,53].

In three dimensions, we have access to an additional HOT phase, namely TOTI, for $\alpha,\ \beta \neq 0$ as compared to the 2D case with $\alpha \neq 0$ only, where one can reach the SOTI. We point out this hierarchy one by one. In the absence of the Wilson-Dirac masses, i.e., $\alpha = \beta = 0$, $H_{3D}^{\text{Static}}(\mathbf{k})$ hosts gapless 2D surface states in the strong TI phase provided $0 < |J_1'| < 3|J_2'|$ [11,61,69]. In addition to the 3D TI phase, if we allow α to be nonzero, the surface states of the underlying TI are gapped out by the corresponding term, and we procure gapless states along the 1D hinge of the system in the z-direction [13,17,61,69]. This is the signature of a 3D SOTI. On the other hand, in the presence of nonzero values of α and β, the first-order 3D TI phase transmutes into a 3D TOTI, harboring 0D corner modes [13,61,69].

B. Periodic mass kick

In our periodic kick protocol, we consider the Hamiltonian $\mathcal{H}_{d\text{D}}$ in d-dimension between two successive kicks. Afterwards, we introduce the driving protocol in the form of an on-site mass kick as

$$m_0(t) = m\, h_{1,d\text{D}} \sum_{r=1}^{\infty} \delta(t - rT), \tag{4}$$

where m denotes the strength of the kicking parameter, t denotes time, and T symbolizes the time period of the drive. Following the periodic kick, we can write down the exact Floquet operator $U_{d\text{D}}(\mathbf{k}, T)$ using the time-ordered ($\overline{\text{TO}}$) notation as

$$\begin{aligned} U_{d\text{D}}(\mathbf{k}, T) &= \overline{\text{TO}} \exp\left[-i \int_0^T dt[\mathcal{H}_{d\text{D}}(\mathbf{k}) + m_0(t)]\right] \\ &= \exp\left(-i\mathcal{H}_{d\text{D}}(\mathbf{k})T\right) \exp(-im\, h_{1,d\text{D}}). \end{aligned} \tag{5}$$

We choose $\mathcal{H}_{2\text{D}}(\mathbf{k}) = J' h_{2,2\text{D}}(\mathbf{k})$ in two dimensions and $\mathcal{H}_{3\text{D}}(\mathbf{k}) = J' h_{2,3\text{D}}(\mathbf{k})$ in three dimensions. Also, $h_{1,2\text{D}}$ $h_{1,3\text{D}}$ were defined earlier. Here, J' carries the dimension of energy. However we use the dimensionless parameter $J = J'T$ along with m to control the drive. Similar to Eqs. (2) and (3), one can obtain the analogous static Hamiltonian for this case as $H_{d\text{D}}^{\text{Static}}(\mathbf{k}) = m\, h_{1,d\text{D}} + J' h_{2,d\text{D}}(\mathbf{k})$. Note that one can achieve the mass kick [Eq. (4)] protocol from the limiting case of the step drive protocol [Eq. (1)] with infinitesimal duration of the first step Hamiltonian $J_1' h_{1,d\text{D}}$.

III. ANOMALOUS DYNAMICAL MODES

Here we present our key findings regarding the generation of dynamical FHOTI phases in two and three dimensions, employing the step drive and periodic mass kick protocols.

A. Step drive

Within the step drive protocol, we can generate the jets of FFOTI, FSOTI, and FTOTI by tuning some specific parameters, which we discuss in the upcoming subsections in detail.

1. Two dimensions

To begin with two dimensions, following step drive protocol, we can write down the full Floquet evolution operator $U_{2\text{D}}(\mathbf{k}, T)$ after one full period T as

$$U_{2\text{D}}(\mathbf{k}, T) = \exp\left(-i\frac{J_2}{2} h_{2,2\text{D}}(\mathbf{k})\right) \exp\left(-i\frac{J_1}{2} h_{1,2\text{D}}(\mathbf{k})\right), \tag{6}$$

where we can express $U_{2\text{D}}(\mathbf{k}, T)$ as $U_{2\text{D}}(\mathbf{k}, T) = f_{2\text{D}}(\mathbf{k})\mathbb{I} + i g_{2\text{D}}(\mathbf{k})$, such that

$$f_{2\text{D}}(\mathbf{k}) = \cos\left(\gamma_{2\text{D}}(\mathbf{k})\frac{J_1}{2}\right)\cos\left(\lambda_{2\text{D}}(\mathbf{k})\frac{J_2}{2}\right) - \sin\left(\gamma_{2\text{D}}(\mathbf{k})\frac{J_1}{2}\right)\sin\left(\lambda_{2\text{D}}(\mathbf{k})\frac{J_2}{2}\right)\chi_{2\text{D}}(\mathbf{k}), \tag{7}$$

$$\begin{aligned} g_{2\text{D}}(\mathbf{k}) = &-\frac{1}{\gamma_{2\text{D}}(\mathbf{k})\lambda_{2\text{D}}(\mathbf{k})}\sin\left(\gamma_{2\text{D}}(\mathbf{k})\frac{J_1}{2}\right)\sin\left(\lambda_{2\text{D}}(\mathbf{k})\frac{J_2}{2}\right)\eta_{2\text{D}}(\mathbf{k}) - \sin\left(\gamma_{2\text{D}}(\mathbf{k})\frac{J_1}{2}\right)\cos\left(\lambda_{2\text{D}}(\mathbf{k})\frac{J_2}{2}\right)\frac{h_{1,2\text{D}}(\mathbf{k})}{\gamma_{2\text{D}}(\mathbf{k})} \\ &- \cos\left(\gamma_{2\text{D}}(\mathbf{k})\frac{J_1}{2}\right)\sin\left(\lambda_{2\text{D}}(\mathbf{k})\frac{J_2}{2}\right)\frac{h_{2,2\text{D}}(\mathbf{k})}{\lambda_{2\text{D}}(\mathbf{k})}. \end{aligned} \tag{8}$$

Here, we have suppressed the implicit T dependence on $f_{2\text{D}}(\mathbf{k})$ and $g_{2\text{D}}(\mathbf{k})$. We have defined $\gamma_{2\text{D}}(\mathbf{k}) = |h_{1,2\text{D}}(\mathbf{k})|$, $\lambda_{2\text{D}}(\mathbf{k}) = |h_{2,2\text{D}}(\mathbf{k})|$, $\chi_{2\text{D}}(\mathbf{k}) = \frac{\cos k_x + \cos k_y}{\gamma_{2\text{D}}(\mathbf{k})\lambda_{2\text{D}}(\mathbf{k})}$, and $\eta_{2\text{D}}(\mathbf{k}) = \sin k_x \sigma_y s_z - \sin k_y \sigma_x + \alpha(\cos k_x - \cos k_y)\sigma_y s_x$. From the eigenvalue equation for $U_{2\text{D}}(\mathbf{k}, T)$, $U_{2\text{D}}(\mathbf{k}, T)\,|\Psi\rangle = e^{iE(\mathbf{k})}\,|\Psi\rangle$, one obtains the condition

$$\cos E(\mathbf{k}) = f_{2\text{D}}(\mathbf{k}), \tag{9}$$

with each band being twofold-degenerate. Now, the band gap closes at $\mathbf{k} = \mathbf{k}^* = (0, 0)$ or (π, π) for $f_{2\text{D}}(\mathbf{k}^*) = \pm 1$ such that $E(\mathbf{k}^*) = n\pi$, with $n = 0, 1, 2, 3, \ldots$ being an integer. The interesting point to note here is that we can cast $f_{2\text{D}}(\mathbf{k})$ in terms of a single cosine function such as $f_{2\text{D}}(\mathbf{k}^*) = \cos(\gamma_{2\text{D}}(\mathbf{k}^*)\frac{J_1}{2} \pm \lambda_{2\text{D}}(\mathbf{k}^*)\frac{J_2}{2})$. Furthermore, the structure of the $\chi_{2\text{D}}(\mathbf{k}^*)$ term here serves as an essential ingredient to continue with the above analysis. To be precise, at these momentum points, $\gamma_{2\text{D}}(\mathbf{k}^*)$, $\lambda_{2\text{D}}(\mathbf{k}^*)$, and $\chi_{2\text{D}}(\mathbf{k}^*)$ take the following values: $\gamma_{2\text{D}}(0, 0) = \gamma_{2\text{D}}(\pi, \pi) = 1$, $\lambda_{2\text{D}}(0, 0) = \lambda_{2\text{D}}(\pi, \pi) = 2$, and $\chi_{2\text{D}}(0, 0) = -\chi_{2\text{D}}(\pi, \pi) = 1$. These special momentum modes continue to play a pivotal role for dynamics in addition to the static counterpart as given in Eqs. (2) and (3). This enables us to write the right-hand side

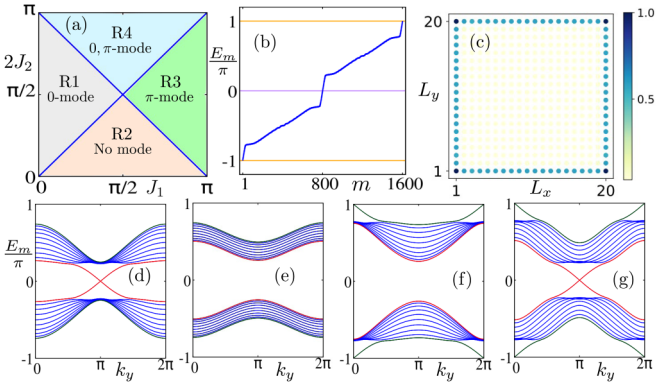

FIG. 1. (a) Phase diagram is depicted in the J_1-J_2 plane for 2D FFOTI, which is guided by Eq. (11). (b) Quasienergy spectrum for a finite system and as a function of the state index m is depicted when the system is in the phase R4. One can clearly identify modes close to quasienergies 0 and $\pm\pi$. (c) The LDOS is shown for a finite-size system corresponding to quasienergies $E_m = 0, \pm\pi$ in R4. The quasienergy spectra E_m, considering slab geometry, for R1, R2, R3, and R4 are shown in panels (d), (e), (f), and (g), respectively. We choose the parameters as $(J_1, 2J_2) = [(\frac{\pi}{4}, \frac{\pi}{2}), (\frac{\pi}{2}, \frac{\pi}{4}), (\frac{3\pi}{4}, \frac{\pi}{2}), (\frac{\pi}{2}, \frac{3\pi}{4})]$ for R1, R2, R3, and R4, respectively.

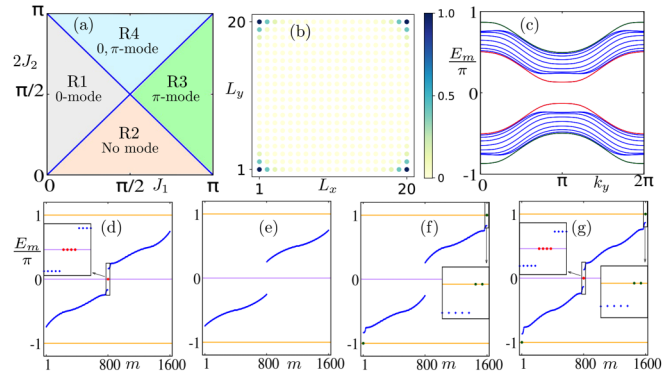

FIG. 2. (a) Phase diagram is demonstrated in the J_1-J_2 plane for 2D FSOTI. (b) LDOS is shown for a finite-size system corresponding to quasienergies $E_m = 0, \pm\pi$ in R4. (c) Quasienergy spectrum E_m, considering slab geometry for our system, is depicted as a function of k_y for R4. One can observe that both the 0 and π edge modes are gapped out due to inclusion of the Wilson-Dirac mass term α. The quasienergy spectra E_m for the finite-size system, corresponding to R1, R2, R3, and R4, are presented as a function of the state index m in panels (d), (e), (f), and (g), respectively. We use the same parameters as mentioned in Fig. 1.

(RHS) of Eq. (7) in a compact form as

$$\cos\left(\frac{J_1}{2} \pm J_2\right) = \cos n\pi, \tag{10}$$

where n is an integer. From Eq. (10), we obtain the gap closing conditions in terms of the dimensionless parameters J_1 and J_2 as

$$|J_2| = \frac{|J_1|}{2} + n\pi. \tag{11}$$

Here, Eq. (11) signifies the topological phase boundaries between various dynamic phases, as depicted in Figs. 1(a) and 2(a). The phase boundaries divide the phase diagram into four parts: region 1 (R1) with 0 mode, region 2 (R2) with no modes, region 3 (R3) with π mode, and region 4 (R4) hosting both 0 and π modes. Interestingly, the phase boundaries remain the same for both FFOTI and FSOTI due to the absence of any α-dependent term in Eq. (11). Instead of considering a two step drive, one can also think about a three step drive protocol as discussed in Ref. [57] and end up obtaining a relation akin to Eq. (11). The underlying reason for this can be attributed to the fact that the structure of $f_{2D}(\mathbf{k}^*)$ remains unaltered in both cases. With the help of Eqs. (6), (7), and (8), we can write the Floquet effective Hamiltonian $H_{2D,Flq}$ as

$$H_{2D,Flq} = -\frac{\epsilon_{2D}(\mathbf{k})}{\sin[\epsilon_{2D}(\mathbf{k})T]} g_{2D}(\mathbf{k}), \tag{12}$$

where $\epsilon_{2D}(\mathbf{k}) = \frac{1}{T}\cos^{-1}[f_{2D}(\mathbf{k})]$.

Note that the ladder of FHOTI including FFOTI can be engineered by selectively incorporating the Wilson-Dirac masses in $h_{2,2D}(\mathbf{k})$. To be precise, $\alpha = 0$ ($\alpha \neq 0$) in $h_{2,2D}(\mathbf{k})$ leads to the FFOTI (FSOTI) phases. After obtaining an analytical understanding of the emergence of the FFOTI and FSOTI phases, we further support our findings by numerical analysis for finite-size systems (see the text for discussion of Case 1 and Case 2).

Case 1: FFOTI. As mentioned earlier, in order to obtain the FFOTI phase, we set $\alpha = 0$. The FFOTI is characterized by the presence of gapless edge modes at its 1D boundary. To uncover the subsistence of gapless *dispersive* edge modes, we resort to slab geometry, i.e., the periodic boundary condition (PBC) along one direction (say y) and the open boundary condition (OBC) in the other direction (say x). We numerically diagonalize the Floquet operator $U_{2D}(k_y, T)$ and depict the quasienergy spectrum as a function of k_y for regions R1, R2, R3, and R4 in Figs. 1(d), 1(e), 1(f), and 1(g), respectively. It is evident that the gapless modes appear at $k_y = 0, \pi$ as discussed earlier in the mathematical analysis. With reference to the phase diagram, Fig. 1(a), obtained analytically from Eq. (11) and verified numerically from $U_{2D}(k_y, T)$ [Eq. (6)], one can observe only 0 mode, no mode, only π mode, and both 0 and π modes in R1, R2, R3, and R4, respectively. The real-space quasienergy spectrum associated with R4 is depicted in Fig. 1(b). There one can identify the FFOTI modes at both $E_m = 0$ and $E_m = \pm\pi$. As discussed above, one expects to notice FFOTI modes separately at $E_m = 0$ ($E_m = \pm\pi$) for R1 (R3) and no modes either at $E_m = 0$ or $E_m = \pi$ for R2, although we prefer not to show them here. The local density of states (LDOS) for a system with OBC in both directions is illustrated in Fig. 1(c) for quasistates with $E_m = 0, \pm\pi$ (within numerical accuracy) corresponding to R4. The LDOS remains unaltered for quasistates corresponding to $E_m = 0$ (R1) and $E_m = \pm\pi$ (R3). These $E_m = \pm\pi$ (at frequency $\pm\Omega/2$) gapless modes refer to the dynamical ones as reported earlier for other systems with different driving schemes [78,79].

Case 2: FSOTI. Turning our focus to the 2D FSOTI phase, which can be obtained by considering $\alpha \neq 0$, the corresponding phase diagram turns out to be unaltered as depicted in

Fig. 2(a). To probe the footprints of FSOTI via the LDOS, we resort to OBC in both directions. We show the LDOS for quasistates with $E_m = 0, \pm\pi$ in Fig. 2(b). It is evident that corner localized modes appear at quasienergies $E_m = 0, \pm\pi$. The quasienergy spectra are shown in Figs. 2(d), 2(e) 2(f), and 2(g) for the phase R1, R2, R3, and R4, respectively. As mentioned earlier, when we set α to be nonzero, the 1D edge modes of FFOTI should be gapped out by the Wilson-Dirac mass term $(\cos k_x - \cos k_y)$, and the corresponding $0, \pi$ modes appear at the corners of the system. This is clearly visible for the present case while comparing Fig. 1(g) with Fig. 2(c), where we depict the gapped edge mode in R4 employing slab geometry. Note that there exist four (two) quasistates at quasienergy $E_m = 0, (\pm\pi)$ for the 2D FSOTI phase.

2. Three dimensions

In three dimensions, we comprehensively unveil how to systematically generate the cascade of FFOTI, FSOTI, and FTOTI phases by suitably tuning the Wilson-Dirac mass perturbations. In three dimensions, the Floquet evolution operator for the step drive protocol reads

$$U_{3D}(\mathbf{k}, T) = \exp\left(-i\frac{J_2}{2}h_{2,3D}(\mathbf{k})\right)\exp\left(-i\frac{J_1}{2}h_{1,3D}(\mathbf{k})\right). \quad (13)$$

Similar to the 2D case, one can find the Floquet evolution operator $U_{3D}(\mathbf{k}, T)$ as $U_{3D}(\mathbf{k}, T) = f_{3D}(\mathbf{k})\mathbb{I} + ig_{3D}(\mathbf{k})$, with

$$f_{3D}(\mathbf{k}) = \cos\left(\gamma_{3D}(\mathbf{k})\frac{J_1}{2}\right)\cos\left(\lambda_{3D}(\mathbf{k})\frac{J_2}{2}\right) - \sin\left(\gamma_{3D}(\mathbf{k})\frac{J_1}{2}\right)\sin\left(\lambda_{3D}(\mathbf{k})\frac{J_2}{2}\right)\chi_{3D}(\mathbf{k}), \quad (14)$$

$$g_{3D}(\mathbf{k}) = -\frac{1}{\gamma_{3D}(\mathbf{k})\lambda_{3D}(\mathbf{k})}\eta_{3D}(\mathbf{k})\sin\left(\gamma_{3D}(\mathbf{k})\frac{J_1}{2}\right)\sin\left(\lambda_{3D}(\mathbf{k})\frac{J_2}{2}\right) - \sin\left(\gamma_{3D}(\mathbf{k})\frac{J_1}{2}\right)\cos\left(\lambda_{3D}(\mathbf{k})\frac{J_2}{2}\right)\frac{h_{1,3D}(\mathbf{k})}{\gamma_{3D}(\mathbf{k})}$$
$$- \cos\left(\gamma_{3D}(\mathbf{k})\frac{J_1}{2}\right)\sin\left(\lambda_{3D}(\mathbf{k})\frac{J_2}{2}\right)\frac{h_{2,3D}(\mathbf{k})}{\lambda_{3D}(\mathbf{k})}, \quad (15)$$

where $\gamma_{3D}(\mathbf{k}) = |h_{1,3D}(\mathbf{k})|$, $\lambda_{3D}(\mathbf{k}) = |h_{2,3D}(\mathbf{k})|$, $\chi_{3D}(\mathbf{k}) = \frac{\cos k_x + \cos k_y + \cos k_z}{\gamma_{3D}(\mathbf{k})\lambda_{3D}(\mathbf{k})}$, and $\eta_{3D}(\mathbf{k}) = \sin k_x\sigma_y s_x + \sin k_y\sigma_y s_y + \sin k_z\sigma_y s_z - \alpha(\cos k_x - \cos k_y)\sigma_x - \beta(2\cos k_z - \cos k_x - \cos k_y)\mu_y\sigma_z$. From the eigenvalue equation of $U_{3D}(\mathbf{k}, T)$, $U_{3D}(\mathbf{k}, T)|\Psi\rangle = e^{iE(\mathbf{k})}|\Psi\rangle$, one obtains

$$\cos E(\mathbf{k}) = f_{3D}(\mathbf{k}), \quad (16)$$

with each band being fourfold-degenerate. Now, the band gap closes at $\mathbf{k} = \mathbf{k}^* = (0, 0, 0)$ or (π, π, π) when $f_{3D}(\mathbf{k}) = \pm 1$. At these points, $\gamma_{3D}(\mathbf{k})$, $\lambda_{3D}(\mathbf{k})$, and $\chi_{3D}(\mathbf{k})$ take the following values: $\gamma(0, 0, 0) = \gamma(\pi, \pi, \pi) = 1$, $\lambda(0, 0, 0) = \lambda(\pi, \pi, \pi) = 3$, and $\chi(0, 0, 0) = -\chi(\pi, \pi, \pi) = 1$. This enables us to write the right-hand side of Eq. (14), following a similar line of arguments discussed for the 2D case, as

$$\cos\left(\frac{J_1}{2} \pm \frac{3J_2}{2}\right) = \cos n\pi. \quad (17)$$

From the above relation [Eq. (17)], we obtain the gap closing relations in terms of J_1 and J_2 as

$$\frac{3|J_2|}{2} = \frac{|J_1|}{2} + n\pi, \quad (18)$$

where n is an integer. Note that Eq. (18) serves the purpose of a topological phase boundary in the 3D case. It is worth mentioning here that the phase diagrams in the J_1-J_2 plane that can obtain different types of first- and higher-order modes remain the same for FFOTI, FSOTI, and FTOTI [see Figs. 3(a), 4(a), and 5(a), respectively]. This can be attributed to the fact that gap-closing conditions are independent of α and β. This is a generic feature of this particular driving protocol. However, the special structures of $\chi_{3D}(\mathbf{k}^*)$ and $f_{3D}(\mathbf{k}^*)$ are held responsible for the above robust nature of these phase diagrams, although, depending upon the choice of the driving scheme, one can obtain the FHOTI phase diagram as a function of mass terms α and β. Using Eqs. (13), (14), and (15), we can write the Floquet effective Hamiltonian $H_{3D,Flq}$ as

$$H_{3D,Flq} = -\frac{\epsilon_{3D}(\mathbf{k})}{\sin[\epsilon_{3D}(\mathbf{k})T]}g_{3D}(\mathbf{k}), \quad (19)$$

where $\epsilon_{3D}(\mathbf{k}) = \frac{1}{T}\cos^{-1}[f_{3D}(\mathbf{k})]$.

Similar to the earlier case for the 2D system, below we explore systematically the emergence of FFOTI and FHOTI phases by numerically diagonalizing the Floquet operator [Eq. (13)] implementing appropriate finite geometries.

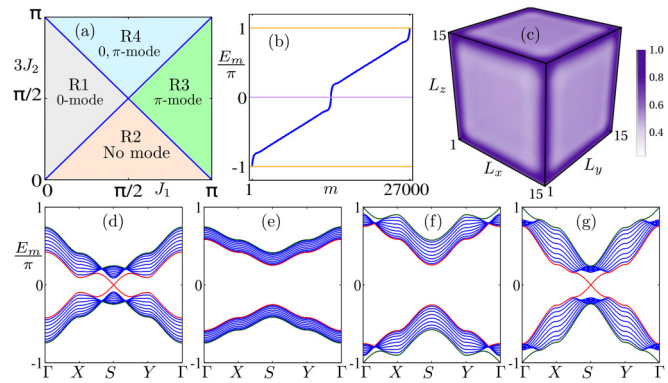

FIG. 3. (a) Phase diagram is depicted in the J_1-J_2 plane for 3D FFOTI. (b) Quasienergy spectrum E_m for a finite-size system is shown as a function of the state index m when the system is in phase R4. (c) LDOS is depicted for a finite-size system corresponding to quasienergies $E_m = 0, \pm\pi$ for R4. The quasienergy spectra E_m considering slab geometry, along the $\Gamma - X - S - Y - \Gamma$ points, for R1, R2, R3, and R4, are shown in panels (d), (e), (f), and (g), respectively. The chosen parameters are $(J_1, 3J_2) = [(\frac{\pi}{4}, \frac{\pi}{2}), (\frac{\pi}{2}, \frac{\pi}{4}), (\frac{3\pi}{4}, \frac{\pi}{2}), (\frac{\pi}{2}, \frac{3\pi}{4})]$ for R1, R2, R3, and R4, respectively.

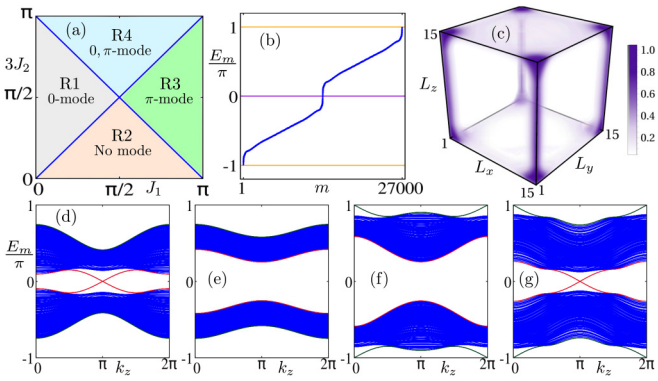

FIG. 4. (a) We demonstrate the phase diagram in the J_1-J_2 plane for 3D FSOTI. (b) Quasienergy spectrum E_m for a finite system is shown as a function of the state index m for R4. (c) The corresponding LDOS is depicted considering quasistates with $E_m = 0, \pm\pi$ in R4. The quasienergy spectra E_m in rod geometry along k_z, corresponding to R1, R2, R3, and R4, are shown in panels (d), (e), (f), and (g), respectively. The parameters are chosen to be the same as in Fig. 3.

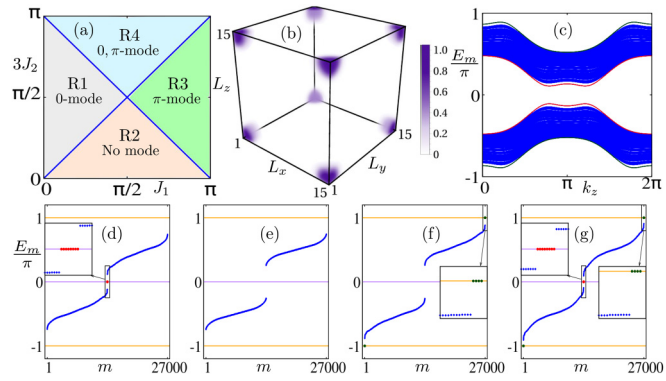

FIG. 5. (a) We illustrate the phase diagram in the J_1-J_2 plane for 3D FTOTI. (b) Corner localized modes corresponding to quasienergies $E_m = 0, \pm\pi$ are shown via LDOS for a finite-size system in R4. (c) Quasienergy spectrum E_m for the system in rod geometry is depicted as a function of k_z, manifesting in the hinge modes (both 0 and $\pm\pi$) being gapped out. The quasienergy spectra E_m for a finite-size system and as a function of the state index m, corresponding to R1, R2, R3, and R4, are shown in panels (d), (e), (f), and (g), respectively. We choose the same parameter values as mentioned in Fig. 3.

Case 1: FFOTI. To obtain the FFOTI phase in three dimensions, we set both $\alpha = 0$ and $\beta = 0$. The FFOTI phase is characterized by the appearance of gapless 2D surface states. The quasienergy spectra for a finite-size system with OBC along the x-, y-, and z-directions, residing in R4, is shown in Fig. 3(b) as a function of the state index m. We depict the signature of the surface states in the LDOS corresponding to quasistates with $E_m = 0, \pm\pi$ for R4 in Fig. 3(c). For a better understanding of the nature of the surface states, we employ slab geometry by considering OBC along one direction (say, the z-direction) while the remaining two directions obey PBC (say, the x- and y-directions). We depict the gapless surface states along $\Gamma - X - S - Y - \Gamma$ points for R1, R2, R3, and R4 in Figs. 3(d), 3(e) 3(f), and 3(g), respectively. Here, $\Gamma = (0, 0)$, $X = (\pi, 0)$, $S = (\pi, \pi)$, $Y = (0, \pi)$.

Case 2: FSOTI. To realize the FSOTI phase, we set α to a nonzero value while keeping $\beta = 0$. We first explore the quasienergy spectra under OBC in all directions as shown in Fig. 4(b), where the existence of both 0 and π modes in R4 is clearly visible as a function of the state index m. We further illustrate the LDOS corresponding to quasistates with $E_m = 0, \pm\pi$ for R4 in Fig. 4(c). One can notice that the mode is populated throughout the hinge along the z-direction of the system. To exhibit the dispersive nature of the gapless hinge modes, we use rod geometry, i.e., considering OBC in two directions (x- and y-directions) and PBC in the remaining direction (z-direction). The corresponding quasienergy spectra for this system are shown in the rod geometry for R1, R2, R3, and R4 in Figs. 4(d), 4(e), 4(f), and 4(g), respectively. These numerical findings can be analytically understood as well from the bulk. The first Wilson-Dirac mass term proportional to $(\cos k_x - \cos k_y)$ is able to gap out the surface modes over all three xy, yz, and zx surfaces except along $x = \pm y$ for any value of z [61].

Case 3: FTOTI. The FTOTI phase can further be obtained when both the mass terms α and β are nonzero. The corresponding phase diagram in the J_1-J_2 plane is shown in Fig. 5(a). In Fig. 5(b), we further depict the signature of corner modes at $E_m = \pm\pi$ for R4 via the LDOS spectrum. This has been computed considering OBC in all directions. In the FTOTI phase, one obtains 0 or π mode only at the corners of the system, while both surface and hinge modes are gapped out. We show the quasienergy spectrum for this system, employing rod geometry (OBC along the x and y-directions, PBC along the z-direction), in Fig. 5(c) (corresponding to R4). It is evident that both 0 and π hinge modes are gapped out [see Fig. 5(c)]. Therefore, this is in contrast to the FSOTI phase, as shown in Fig. 4(g). The second Wilson-Dirac mass term $\beta(2\cos k_z - \cos k_x - \cos k_y)$ gaps out the hinge mode except at the body diagonal position $\pm z = \pm y = \pm x$ where corner modes appear [61]. The presence of dynamical corner modes can be better understood by exploring the quasienergy spectra for a system obeying OBC in all three directions. We show the corresponding quasienergy spectra as a function of the state index m, employing OBC for R1, R2, R3, and R4 in Figs. 5(d), 5(e), 5(f), and 5(g), respectively. Note that there exist eight (four) quasistates at $E_m = 0, (\pm\pi)$ for the FTOTI phase, which contribute to the corner localized LDOS.

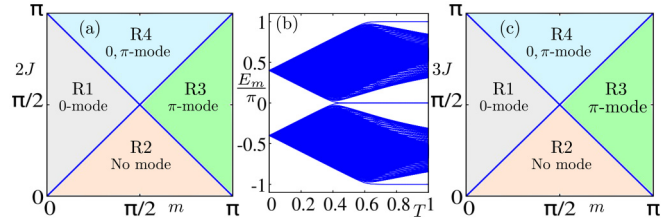

FIG. 6. (a) Phase diagram for the kick driving protocol is depicted in the m-J plane for a 2D FFOTI/FSOTI. (b) Quasienergy spectrum E_m is shown as a function of the driving time period T. This exhibits the $0, \pm\pi$ modes. We choose $(m, J') = (0.4\pi, 0.5\pi)$. (c) The corresponding phase diagram for a 3D FFOTI/FSOTI/FTOTI is illustrated in the m-J plane.

B. Periodic mass kick

After extensive discussion on the hierarchy of FHOTI phases starting from FFOTI phases (under the step drive scheme), we now proceed to analyze our findings for the mass kick protocol as given in Eq. (4). In the periodic mass kick formalism, the Floquet operator $U_{dD}(\mathbf{k}, T)$ can be cast in the form $U_{dD}(\mathbf{k}, T) = f_{dD}(\mathbf{k})\mathbb{I} + ig_{dD}(\mathbf{k})$, with

$$f_{2D}(\mathbf{k}) = \cos[\gamma_{2D}(\mathbf{k})m]\cos[\lambda_{2D}(\mathbf{k})J] - \sin[\gamma_{2D}(\mathbf{k})m]\sin[\lambda_{2D}(\mathbf{k})J]\chi_{2D}(\mathbf{k}), \tag{20}$$

$$g_{2D}(\mathbf{k}) = -\frac{1}{\gamma_{2D}(\mathbf{k})\lambda_{2D}(\mathbf{k})}\eta_{2D}(\mathbf{k})\sin[\gamma_{2D}(\mathbf{k})m]\sin[\lambda_{2D}(\mathbf{k})J] - \sin[\gamma_{2D}(\mathbf{k})m]\cos[\lambda_{2D}(\mathbf{k})J]\frac{h_{1,2D}(\mathbf{k})}{\gamma_{2D}(\mathbf{k})} - \cos[\gamma_{2D}(\mathbf{k})m]\sin[\lambda_{2D}(\mathbf{k})J]\frac{h_{2,2D}(\mathbf{k})}{\lambda_{2D}(\mathbf{k})}, \tag{21}$$

$$f_{3D}(\mathbf{k}) = \cos[\gamma_{3D}(\mathbf{k})m]\cos[\lambda_{3D}(\mathbf{k})J] - \sin[\gamma_{3D}(\mathbf{k})m]\sin[\lambda_{3D}(\mathbf{k})J]\chi_{3D}(\mathbf{k}), \tag{22}$$

$$g_{3D}(\mathbf{k}) = -\frac{1}{\gamma_{3D}(\mathbf{k})\lambda_{3D}(\mathbf{k})}\eta_{3D}(\mathbf{k})\sin[\gamma_{3D}(\mathbf{k})m]\sin[\lambda_{3D}(\mathbf{k})J] - \sin[\gamma_{3D}(\mathbf{k})m]\cos[\lambda_{3D}(\mathbf{k})J]\frac{h_{1,3D}(\mathbf{k})}{\gamma_{3D}(\mathbf{k})} - \cos[\gamma_{3D}(\mathbf{k})m]\sin[\lambda_{3D}(\mathbf{k})J]\frac{h_{2,3D}(\mathbf{k})}{\lambda_{3D}(\mathbf{k})}, \tag{23}$$

where the mathematical symbols carry the same definitions as before. Thus, the Floquet effective Hamiltonians for 2D and 3D systems can be obtained as

$$H_{2D,Flq} = -\frac{\epsilon_{2D}(\mathbf{k})}{\sin[\epsilon_{2D}(\mathbf{k})T]}g_{2D}(\mathbf{k}), \tag{24}$$

$$H_{3D,Flq} = -\frac{\epsilon_{3D}(\mathbf{k})}{\sin[\epsilon_{3D}(\mathbf{k})T]}g_{3D}(\mathbf{k}), \tag{25}$$

where $\epsilon_{2D}(\mathbf{k}) = \frac{1}{T}\cos^{-1}[f_{2D}(\mathbf{k})]$ and $\epsilon_{3D}(\mathbf{k}) = \frac{1}{T}\cos^{-1}[f_{3D}(\mathbf{k})]$.

As discussed earlier, the gap closing conditions can be obtained using the right-hand side of Eqs. (20) and (22) in two and three dimensions as

$$2|J| = |m| + n\pi \quad \text{in 2D}, \tag{26}$$

$$3|J| = |m| + n\pi \quad \text{in 3D}. \tag{27}$$

Like the step drive case, the nature of the phase boundary remains the same for all the topological orders in every dimension. To be precise, in two dimensions, the phase boundary for both FFOTI and FSOTI is guided by Eq. (26), whereas, in three dimensions, the same is controlled by Eq. (27). The corresponding phase boundaries for two and three dimensions are shown in Figs. 6(a) and 6(c), respectively.

Here, we intend to compare our findings between mass kick and step drive protocols. The factor $\chi_{2D}(\mathbf{k})$, computed at the high-symmetry point $\mathbf{k} = \mathbf{k}^*$, plays an important role in the case of both drives. This factor eventually allows $f_{2D}(\mathbf{k}^*)$ to acquire a simple form in terms of a single cosine function. Once $\chi_{2D}(\mathbf{k}^*)$ inherits a complicated mathematical form, $f_{2D}(\mathbf{k}^*)$ cannot be written in a compact way. More importantly, in order to observe the regular 0 mode and anomalous π mode together in the driven system, the condition $|\chi_{2D}(\mathbf{k}^*)| = 1$ becomes very important. The condition $E(\mathbf{k}^*) = 0$ [$E(\mathbf{k}^*) = \pm\pi$] yields the condition for obtaining 0 mode (π mode). Another crucial point to note here is that the gap closing transition in the quasienergy spectrum has to take place at the high-symmetry points, i.e., $\mathbf{k} = \mathbf{k}^*$. This is an essential requirement to procure the anomalous FHOTI modes. This further leads to the generic gap-closing condition, as represented by Eqs. (10) and (17), $\cos(E(\mathbf{k}^*)) = (-1)^n$, with $n = 0, 1, 2, 3, \ldots$. Thus the compact form of phase boundaries eventually can be portrayed as $d|J_2| = |J_1| + 2n\pi$ ($d|J| = |m| + n\pi$) for the step drive (mass kick), with d being the dimension. The above discussion is not restricted to any specific driving protocol discussed here, rather it is applicable to a variety of driving schemes [57,63,64].

For completeness, we briefly discuss the numerical results for this particular driving in two and three dimensions. To start with two dimensions, we obtain the FFOTI phase by setting $\alpha = 0$. However, the quasienergy spectra in the slab geometry remain qualitatively the same as those of the step drive case for R1, R2, R3, and R4 phase as depicted in Figs. 1(d), 1(e), 1(f), and 1(g), respectively. To procure the FSOTI, we set α to a nonzero value, and the corresponding quasienergy spectra encompassing the corner modes (at $E_m = 0, \pm\pi$) for a finite-size system turn out to be similar to that shown in Figs. 2(d), 2(e), 2(f), and 2(g) for the sectors R1, R2, R3, and R4, respectively.

In three dimensions, the FFOTI emerges when both α and β are zero. The surface states can be found by realizing the corresponding lattice model in the slab geometry [see Figs. 3(d), 3(e), 3(f), and 3(g)]. The qualitative nature of these surface states remains the same as that obtained implementing the step drive protocol. Furthermore, the system manifests FSOTI hosting gapless hinge modes when $\alpha \neq 0$ but $\beta = 0$. The corresponding signature is highlighted in the quasienergy spectrum that has been calculated using rod geometry [see Figs. 4(d), 4(e), 4(f), and 4(g)]. To obtain the FTOTI phase, both α and β are set to a nonzero value. The footprints of the corner localized modes (at $E_m = 0, \pm\pi$) in the FTOTI phase are found in the quasienergy spectrum for a finite-size system [see Figs. 5(d), 5(e), 5(f), and 5(g)].

One intriguing difference regarding topological phase boundary equations between step drive and periodic kick is the absence of the time period T in the latter case. Importantly, for the step drive the time period T is coupled to both driving

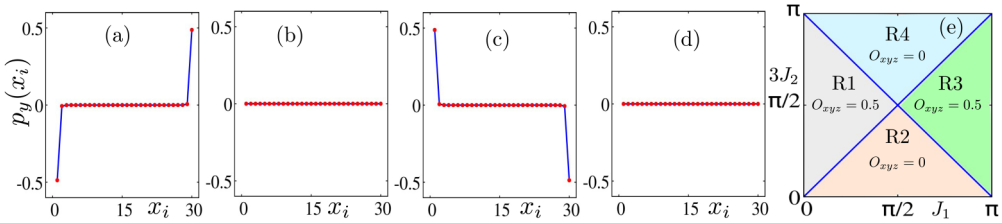

FIG. 7. Tangential polarization $p_y(x_i)$ is demonstrated for FSOTI for R1, R2, R3, and R4 in panels (a), (b), (c), and (d), respectively, choosing the same parameters as in Fig. 2. (e) Octupolar moment O_{xyz} is schematically shown for a 3D FTOTI in the J_1-J_2 plane. $O_{xyz} = 0.5$ in phases R1 and R3, whereas $O_{xyz} = 0.0$ in both phases R2 and R4.

parameters $J'_{1,2}$ such that $J_{1,2}$ becomes the effective parameter to characterize the dynamical system. On the other hand, for periodic kick there exist two effective driving parameters, $J = J'T$ and m, where only one of them is renormalized by T while the other remains unaltered. This, in fact, allows us to seek a frequency driven topological phase transition in the system [see Fig. 6(b)]. We begin with a parameter set: $(m, J') = (0.4\pi, 0.5\pi)$, such that we belong to R2 with no modes. Afterwards, we decrease (increase) the frequency (time period) of the drive while keeping both m and J' fixed. Thus, we move towards R1, where the 0 mode appears, and then to R4, where both the 0 and π modes emerge. Therefore, the topological phase transition, mediated by the driving parameters, is a common feature for step driving [57,63,64], while the kick protocol can further give rise to the frequency driven topological phase transition [42].

IV. TOPOLOGICAL CHARACTERIZATION

The topological protection of corner modes in 2D SOTI can be traced down by the position resolved tangent polarization [14]. Due to the fact that a quadrupole can be thought of in terms of dipole pumping, the fractional corner charge in two dimensions can be traced back to tangential polarization, defined in the semi-infinite geometry with OBC (L_x number of sites) along one of the directions (say, x). Motivated by the above analogy in a static system, we examine the tangential polarization for the driven case to characterize FSOTI [18]. To compute the following, we first construct the Wilson loop operator [14] in the slab geometry (considering PBC along the y-direction and OBC along the x-direction) as $\mathcal{W}_y = F_{y,k_y+(N_y-1)\Delta k_y} \cdots F_{y,k_y+\Delta k_y} F_{y,k_y}$ with $[F_{y,k_y}]_{mn} = \langle \psi_{n,k_y+\Delta k_y} | \psi_{m,k_y} \rangle$, where $\Delta k_y = 2\pi/N_y$ [N_y being the number of discrete points considered inside the Brillouin zone (BZ) along k_y], $|\psi_{m,k_y}\rangle$ is the mth occupied quasienergy state of the Floquet operator $U_{2D}(k_y, T)$, and k_y denotes the base point from where we start to construct the Wilson loop operator.

Then, the $(2N \times 2N)$-dimensional Wannier Hamiltonian $\mathcal{H}_{\mathcal{W}_y}$ can be written as $\mathcal{H}_{\mathcal{W}_y} = -i \ln \mathcal{W}_y$, whose eigenvalues are of the form $2\pi\nu_y$. Here, $\nu_y \equiv \mathrm{mod}(\nu_y, 1)$ is the Wannier center. The position-dependent tangential polarization $p_y(x_i)$ is defined as

$$p_y(x_i) = \frac{1}{2\pi N_y} \sum_{j,k_y,\beta} \left| \sum_{\alpha} [\nu_{j,k_y}]_\alpha [\psi_{\alpha,k_y}]_{\beta,x_i} \right|^2 \nu_{j,y}, \qquad (28)$$

where $[\nu_{j,k_y}]_\alpha$ refers to the αth component of the jth eigenstate $|\nu_{j,k_y}\rangle$ of the Wannier Hamiltonian $\mathcal{H}_{\mathcal{W}_y}$, corresponding to the Wannier center $\nu_{j,y}$. Although the Wanner center $\nu_{j,y}$ is independent of the base point k_y, the eigenstates of the Wannier Hamiltonian do depend on the base point. Here, $[\psi_{\alpha,k_y}]_{\beta,x_i}$ is the (β, x_i)th component of the αth occupied eigenstate $|\psi_{\alpha,k_y}\rangle$ corresponding to the Floquet operator $U_{2D}(k_y, T)$. The index β denotes the combined number of spin and pseudospin degrees of freedom at a lattice site, which is four in the present case.

We depict the behavior of $p_y(x_i)$ as a function of the lattice site x_i in Figs. 7(a), 7(b), 7(c), and 7(d) corresponding to the phase R1, R2, R3, and R4 [see earlier in the text and Fig. 2(a)], respectively. In the R1 and R3 phase, the system exhibits corner modes at quasienergy $E_m = 0$ or $\pm\pi$ [see Figs. 2(d) and 2(f)]. In these cases, the tangential polarization is able to portray the topological nature of corner modes. In particular, the edge polarization, $p_y^{\mathrm{edge}} = \sum_{x_i=1}^{L_x/2} p_y(x_i)$, exhibits a quantized value of 0.5, which is the signature of the second-order topological phase [14], where L_x is the number of lattice sites along the x-direction. In contrast, p_y^{edge} remains at 0 for both the trivial phase R2 and the nontrivial phase R4 (hosting both 0 and $\pm\pi$ modes), and hence we are unable to conclude that there is any apprehensible distinction between them [57]. The dynamical quadrupolar motion introduced in Ref. [57], however, can unambiguously reveal the presence of a corner mode at 0 or π gap. But to evaluate said invariant, mirror symmetry must be present in the system, which is not the case here. Therefore, calculation of a topological indicator for a mirror symmetry broken model system remains an open question.

We emphasize here that the breaking of mirror symmetries in $h_{2,dD}(\mathbf{k})$ severely affects the quadrupole and octupole motion that otherwise can distinguish the regular 0 mode from the anomalous π mode by exhibiting gapless crossing with time and accurately capturing the bulk boundary correspondence for the driven systems [57,80]. The above two quantities serve as the legitimate bulk invariants for the FHOTI phases following the construction of a dynamical nested Wilson loop. We cannot resort to these bulk invariants for their gapped profile due to the absence of mirror symmetry in our case. Therefore, we continue with the edge polarization [Eq. (28)], which turns out to be an inappropriate bulk invariant for dynamics, and thus the bulk boundary correspondence cannot be fully captured for all the dynamical phases discussed here.

For a FTOTI in three dimensions, considering PBC in the real-space geometry, one can calculate the octupole moment,

defined as [81]

$$O_{xyz} = \mathrm{Re}\left[-\frac{i}{2\pi}\mathrm{Tr}\left(\ln\left(\Psi_0^\dagger \exp\left[2\pi i \sum_r \hat{o}_{xyz}(r)\right]\Psi_0\right)\right)\right], \tag{29}$$

where Ψ_0 is the many-body ground state, which we obtain by columnwise arranging the quasienergy states of the Floquet operator $U_{3D}(T)$ according to their quasienergy $-\Omega/2 \leqslant E_m \leqslant 0$: $\Psi_0 = \sum_{m\in E_m\leqslant 0} |\phi_m\rangle\langle\phi_m|$ [53,58,61]. Also, $\hat{o}_{xyz} = \hat{n}(r)xyz/L^3$, with $\hat{n}(r)$ being the number operator at $r = (x, y, z)$.

Note that, for the phase R1 and R3, O_{xyz} exhibits a quantized value of 0.5, where corner modes appear separately at quasienergy $E_m = 0$ and $\pm\pi$, respectively (see Fig. 5), although O_{xyz} cannot discriminate between the phase R2 and R4, manifesting a congruent value of 0. We depict O_{xyz} using a schematic representation in Fig. 7(e). We note that the octupole moment can be considered as the appropriate bulk invariant for the static system. The anomalous mode cannot be appropriately characterized by the same. It might be possible that 0 and π mode interfere destructively yielding 0 (mod 1) as a measure of the invariant. As discussed above, the Floquet operator again turns out to be insufficient for the proper dynamical characterization. Therefore, the octupole moment [Eq. (29)] as well cannot refer to the accurate bulk boundary correspondence for a driven system similar to the edge-polarization [Eq. (28)].

V. DISCUSSIONS AND OUTLOOK

A. Extended phase diagram

First our aim is to generalize the topological phase diagram as displayed in Fig. 2(a). To contemplate the extended phase diagram, we extend the scale of (J_1, J_2) so that one can obtain various phases $|J_2| = |J_1|/2 + n\pi$ with different values of n. We know that there exist four (two) regular 0 (anomalous π, residing at $E_m = +\pi$ or $-\pi$)-modes in the FSOTI phase. By changing the parameter set (J_1, J_2), one can in principle reach several other FSOTI phases where the number of 0 and π modes can be varied. This is extensively demonstrated in Fig. 8. The 0 (π) -gap closings are indicated by the blue (red) lines. As a result, one can clearly see that the dynamical topological phases, separated by blue (red) lines, are hosting an identical number of π (0) modes. The blue (red) lines are associated with $n = 0, 2, 4, \ldots$ ($n = 1, 3, 5, \ldots$) provided J_1, J_2 is positive. More interestingly, this phase diagram is invariant with the time period T as the effective dynamics controlling parameters (J_1, J_2) are both renormalized by the time period T. One can hence think of this extended phase diagram as equally valid for the other step drive protocols [57,63,64]. However, the above discussion is applicable for all the other phase diagrams for the step drive scheme presented in this work. Therefore, in the future it would be an interesting open question to characterize these phases with an appropriate dynamical topological invariant.

B. High-frequency approximation

Having discussed and analyzed our findings at a given frequency, we now present the high-frequency effective Hamiltonians for both driving protocols. In the high-frequency limit, i.e., $T \to 0$, the effective Hamiltonians for two and three dimensions in the case of a step drive and the periodic mass kick boil down to the following form [82]:

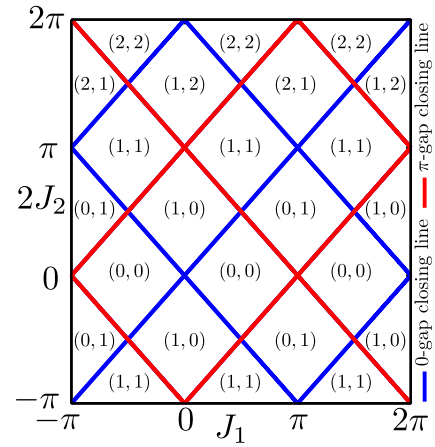

FIG. 8. Extended phase diagram is illustrated in the J_1-J_2 plane in the case of a 2D FFOTI/FSOTI. Here, (i, j) represent the number of 0, π modes present at that parameter regime.

$$H^{\mathrm{eff}}_{2\mathrm{D,step}}(\mathbf{k}) = \frac{J_1'}{2}h_{1,2\mathrm{D}}(\mathbf{k}) + \frac{J_2'}{2}h_{2,2\mathrm{D}}(\mathbf{k}) + \frac{J_1'J_2'T}{4}\eta_{2\mathrm{D}}(\mathbf{k}), \tag{30}$$

$$H^{\mathrm{eff}}_{3\mathrm{D,step}}(\mathbf{k}) = \frac{J_1'}{2}h_{1,3\mathrm{D}}(\mathbf{k}) + \frac{J_2'}{2}h_{2,3\mathrm{D}}(\mathbf{k}) + \frac{J_1'J_2'T}{4}\eta_{3\mathrm{D}}(\mathbf{k}), \tag{31}$$

$$H^{\mathrm{eff}}_{2\mathrm{D,kick}}(\mathbf{k}) = J'h_{2,2\mathrm{D}}(\mathbf{k}) + \frac{m}{T}h_{1,2\mathrm{D}}(\mathbf{k}) + mJ'\eta_{2\mathrm{D}}(\mathbf{k}), \tag{32}$$

$$H^{\mathrm{eff}}_{3\mathrm{D,kick}}(\mathbf{k}) = J'h_{2,3\mathrm{D}}(\mathbf{k}) + \frac{m}{T}h_{1,3\mathrm{D}}(\mathbf{k}) + mJ'\eta_{3\mathrm{D}}(\mathbf{k}). \tag{33}$$

For the mass kick protocol, we also approximate $m \to 0$ such that m/T becomes finite. One can observe that the static Hamiltonians $H^{\mathrm{Static}}_{2\mathrm{D}}(\mathbf{k})$ and $H^{\mathrm{Static}}_{3\mathrm{D}}(\mathbf{k})$ [Eqs. (2) and (3)] resemble the high-frequency effective Hamiltonians $H^{\mathrm{eff}}_{2\mathrm{D,step}}(\mathbf{k})$ and $H^{\mathrm{eff}}_{3\mathrm{D,step}}(\mathbf{k})$ [Eqs. (30) and (31)], except for the appearance of the additional term associated with $\eta_{d\mathrm{D}}(\mathbf{k})$ in the latter case. In the high-frequency limit, the effective Hamiltonians are quasistatic in the sense that no long-range hopping has been incorporated with the inclusion of this additional term proportional to $\eta_{d\mathrm{D}}(\mathbf{k})$. This might allow us to work with the static definition of a topological invariant that is equally trustworthy to characterize the dynamical phases such as the Floquet quadrupole moment [53,58,61,65,66,69]. We note that the 0 mode is expected to survive even in the presence of this extra factor as the effective Hamiltonians preserve particle-hole symmetry: $\mathcal{P}H^{\mathrm{eff}}_{d\mathrm{D},\zeta}(\mathbf{k})\mathcal{P}^{-1} = -H^{\mathrm{eff}}_{d\mathrm{D},\zeta}(-\mathbf{k})$, with $\zeta =$ step, kick [53,83]. Interestingly, with decreasing frequency, different Floquet zones can come closer and that might results into the anomalous π-mode. However, the above statement is not equally applicable to different kinds of driving. It might be useful in the future to analyze the dynamical topological phases, with appropriate topological characterization, in the intermediate frequency range where one can consider $O(T^n)$ for $n > 1$ terms.

C. Other possible driving schemes to engineer FHOTI

We know that one can architect the FFOTI phase by employing laser driving as extensively discussed for 2D lattice systems [36,38,40,79,84,85]. Very recently, the emergence of FSOTI phases in two dimensions has been introduced using laser driving [58]. On the other hand, periodic driving through phonon-mediated spin-orbit coupling is shown to exhibit the FSOTI phase when the underlying static system has reflection symmetry [86]. The manipulation of TRS using the Floquet-Zeeman term becomes instrumental to experience the Floquet second-order topological superconductor phase [87]. The role of mirror symmetry is also emphasized in order to achieve the FSOTI phase [56]. Having discussed a handful of examples including C_4 symmetry breaking perturbations [17,53], we can comment that only a few of the available dynamical protocols are able to produce the anomalous π mode in the FHOTI phases. In this context, the gap-structure of the quasienergy spectrum at the high-symmetry point might become very important, as we discussed previously. Our approach is successfully able to portray the series of FHOTI phases, FFOTI $\rightarrow$ FSOTI $\rightarrow$ FTOTI, while incorporating different symmetry-breaking terms only in one of the steps (midkick) Hamiltonian for the step (kick) protocol. In the present case, the Floquet operator satisfies antiunitary symmetry $\mathcal{P}U_{d\mathrm{D}}(\mathbf{k},T)\mathcal{P}^{-1} = U_{d\mathrm{D}}(-\mathbf{k},T)$, referring to the fact that the 0 and π modes in the FFOTI and FHOTI phases are protected by the particle-hole symmetry [88]. It remains an open question how one can engineer the hierarchy of FHOTI phases (hosting dynamical π modes) in three dimensions employing other drive protocols (e.g., laser driving).

We now compare our findings with another related work where systematic generation of regular FHOTI phases with zero quasienergy modes has been demonstrated [61]. The periodic kick with high frequency, compared to the bandwidth of the system, in the Wilson-Dirac mass term there leads to the zero quasienergy Floquet hinge and corner modes. A quantitative investigation, adopted from a specific case with the kick in the second-order Wilson-Dirac mass term $V_1 = \sqrt{3}\Delta_1(\cos k_x - \cos k_y)$ ($\Delta_1 < t_0$), suggests that to observe regular FHOTI phase with zero quasienergy, the time period T has to be small compared to the bandwidth of the static system, with t_0 and m being the hopping amplitude and the first-order mass term, respectively. Interestingly, the anomalous phase (with π mode) cannot be embedded in the high-frequency phase diagram following the above-mentioned drive protocol [61]. This is in stark contrast to our present case with the step drive protocol where all four dynamic phases R1, R2, R3, and R4 have emerged irrespective of the frequency regime.

Having compared the various examples of Floquet engineering of HOT phases, we now highlight the structural tunability of Floquet hinge modes. It has been shown that the SOTI phase in three dimensions can host connected hinge modes, preserved by a nonsymmorphic space-time symmetry, namely time glide symmetry, under harmonic drive [59]. To be precise, the hinge modes are localized at the intersections of the two sets of surfaces that are related by the reflection part of the time-glide symmetry. The harmonic drive induces opposite masses in these sets of surfaces, leading to a connected hinge at their intersections along the $\tilde{x}$-, $\tilde{z}$-, and $\tilde{y}$-directions provided the crystal cuts are not along the principal axes. We do not encounter such hinge modes in our case, where four disconnected hinge modes appear only along the z-direction as xz- and yz-surfaces are gapped out with opposite mass terms. Therefore, the SOTI is manufactured out of the FOTI by gapping out the surface modes except at the hinges in three dimensions due to the Wilson-Dirac mass term $(\cos k_x - \cos k_y)\mu_x\sigma_y$ [17,21,61,66]. Importantly, the SOTI phase is preserved by $C_4\mathcal{T}$ symmetry. The above mechanism also holds for the FSOTI phase as long as lattice termination remains compatible with the C_4 symmetry, respecting the principal axes. The Floquet dynamics can be simply understood by the fact that the FFOTI is elevated to FSOTI followed by FTOTI while the HOT mass terms are appropriately incorporated in $h_{2,3\mathrm{D}}(\mathbf{k})$. Therefore, one can in principle engineer disconnected and connected hinge modes by suitably choosing the Wilson-Dirac mass and/or Floquet driving and/or lattice configuration.

D. Effect of disorder

In recent years, the disorder mediated HOTI phases have attracted significant attention [89–92]. In particular, random on-site disorder in a 2D system, with chiral symmetry, can induce a quadrupolar topological insulating phase with interesting localization properties [90]. On the the hand, for driven systems, the concept of a Floquet Anderson insulator is introduced where a topologically protected nonequilibrium transport phenomenon is observed [93,94]. In this context, the effect of weak disorder has been investigated in a Floquet quasistatic second-order topological superconductor phase [66]. This is an emerging field of research where strong disorder effects can lead to significantly different phenomena in the context of FHOTI phases [95,96]. The appropriate definition of topological invariant would become very important to characterize these phases; this remains an open field of research.

VI. SUMMARY AND CONCLUSION

To summarize, in this article we consider simple periodic drive protocols, and we illustrate the systematic generation of a series of FHOTI phases including the FFOTI phase, both in two and three dimensions. To begin with, we consider the two-step drive protocol, in which the first half is comprised of on-site terms only and the second half contains all the off-diagonal hopping terms. With such an admixture of tight-binding Hamiltonians, we first show the appearance of the FFOTI phase in the absence of discrete symmetry-breaking Wilson-Dirac mass terms. Upon systematic inclusion of these terms in the second step Hamiltonian, we obtain the FSOTI followed by FTOTI phases in three dimensions. In the process, we also exemplify the 2D case in which one can reach up to corner modes in the FSOTI phase. Most interestingly, we find the regular quasistatic 0 mode, similar to the static case, as well as the anomalous (dynamical) π mode, unlike the static case, in all the above phases. We study analytically the evolution operator and the corresponding topological phase diagram, consisting of 0, π, 0-π-modes in a different parameter regime. The latter is successfully explained

by the appropriate gap closing conditions from the evolution operator. We support our analytical findings by numerical computation for a finite-size system with appropriate boundary conditions. We further continue with another driving scheme, namely mass kick, to recheck the robustness of the above findings. The qualitatively identical phase diagram, obtained under the above driving scheme, can be attributed to the special structure of the identity term in the evolution operator at the high symmetry points. Most interestingly, the number of 0 and π modes can vary in the step drive case, while a frequency-driven topological phase transition is witnessed for the mass kick protocol. We employ tangential polarization (a Floquet octupolar moment) to characterize topologically the FSOTI (FTOTI) in two (three) dimensions with either 0 or $\pm\pi$ corner modes. However, our topological inviariants are incapable of characterizing the dynamical phase hosting the regular 0 and the anomalous π mode simultaneously.

In recent times, significant experimental advancement has been made in the case of HOTI based on solid-state materials [70,71], acoustic systems [72,73,97,98], classical electrical circuits [76], etc, although the experimental observation of FHOTI phases in two and three dimensions is still in its infancy [99]. Nevertheless, given the experimental progress in this research field, we believe that our theoretical model and driving protocols to generate the series of FHOTI phases (anchoring 0 and π modes) are timely and could potentially be realized in future experiments. However, an exact description of experimental techniques and a prediction of candidate material are not the subjects of our present manuscript.

ACKNOWLEDGMENTS

A.K.G. and A.S. acknowledge SAMKHYA: High-Performance Computing Facility provided by Institute of Physics, Bhubaneswar, for numerical computations. T.N. acknowledges Bitan Roy for useful discussions.

[1] K. V. Klitzing, G. Dorda, and M. Pepper, New Method for High-Accuracy Determination of the Fine-Structure Constant Based on Quantized Hall Resistance, Phys. Rev. Lett. **45**, 494 (1980).

[2] D. J. Thouless, M. Kohmoto, M. P. Nightingale, and M. den Nijs, Quantized Hall Conductance in a Two-Dimensional Periodic Potential, Phys. Rev. Lett. **49**, 405 (1982).

[3] F. D. M. Haldane, Model for a Quantum Hall Effect without Landau Levels: Condensed-Matter Realization of the "Parity Anomaly", Phys. Rev. Lett. **61**, 2015 (1988).

[4] C. L. Kane and E. J. Mele, Quantum Spin Hall Effect in Graphene, Phys. Rev. Lett. **95**, 226801 (2005).

[5] J. E. Moore and L. Balents, Topological invariants of time-reversal-invariant band structures, Phys. Rev. B **75**, 121306(R) (2007).

[6] R. Roy, Z_2 classification of quantum spin Hall systems: An approach using time-reversal invariance, Phys. Rev. B **79**, 195321 (2009).

[7] B. A. Bernevig, T. L. Hughes, and S.-C. Zhang, Quantum spin hall effect and topological phase transition in hgte quantum wells, Science **314**, 1757 (2006).

[8] M. Z. Hasan and C. L. Kane, Colloquium: Topological insulators, Rev. Mod. Phys. **82**, 3045 (2010).

[9] X.-L. Qi and S.-C. Zhang, Topological insulators and superconductors, Rev. Mod. Phys. **83**, 1057 (2011).

[10] M. König, S. Wiedmann, C. Brüne, A. Roth, H. Buhmann, L. W. Molenkamp, X.-L. Qi, and S.-C. Zhang, Quantum spin hall insulator state in hgte quantum wells, Science **318**, 766 (2007).

[11] H. Zhang, C.-X. Liu, X.-L. Qi, X. Dai, Z. Fang, and S.-C. Zhang, Topological insulators in Bi_2Se_3, Bi_2Te_3 and Sb_2Te_3 with a single dirac cone on the surface, Nat. Phys. **5**, 438 (2009).

[12] D. Hsieh, D. Qian, L. Wray, Y. Xia, Y. S. Hor, R. J. Cava, and M. Z. Hasan, A topological dirac insulator in a quantum spin hall phase, Nature (London) **452**, 970 (2008).

[13] W. A. Benalcazar, B. A. Bernevig, and T. L. Hughes, Quantized electric multipole insulators, Science **357**, 61 (2017).

[14] W. A. Benalcazar, B. A. Bernevig, and T. L. Hughes, Electric multipole moments, topological multipole moment pumping, and chiral hinge states in crystalline insulators, Phys. Rev. B **96**, 245115 (2017).

[15] Z. Song, Z. Fang, and C. Fang, $(d-2)$-Dimensional Edge States of Rotation Symmetry Protected Topological States, Phys. Rev. Lett. **119**, 246402 (2017).

[16] J. Langbehn, Y. Peng, L. Trifunovic, F. von Oppen, and P. W. Brouwer, Reflection-Symmetric Second-Order Topological Insulators and Superconductors, Phys. Rev. Lett. **119**, 246401 (2017).

[17] F. Schindler, A. M. Cook, M. G. Vergniory, Z. Wang, S. S. P. Parkin, B. A. Bernevig, and T. Neupert, Higher-order topological insulators, Science Adv. **4**, eaat0346 (2018).

[18] S. Franca, J. van den Brink, and I. C. Fulga, An anomalous higher-order topological insulator, Phys. Rev. B **98**, 201114(R) (2018).

[19] Z. Wang, B. J. Wieder, J. Li, B. Yan, and B. A. Bernevig, Higher-Order Topology, Monopole Nodal Lines, and the Origin of Large Fermi Arcs in Transition Metal Dichalcogenides $x\text{te}_2$ (x = Mo, W), Phys. Rev. Lett. **123**, 186401 (2019).

[20] M. Ezawa, Higher-Order Topological Insulators and Semimetals on the Breathing Kagome and Pyrochlore Lattices, Phys. Rev. Lett. **120**, 026801 (2018).

[21] D. Călugăru, V. Juričić, and B. Roy, Higher-order topological phases: A general principle of construction, Phys. Rev. B **99**, 041301(R) (2019).

[22] L. Trifunovic and P. W. Brouwer, Higher-Order Bulk-Boundary Correspondence for Topological Crystalline Phases, Phys. Rev. X **9**, 011012 (2019).

[23] E. Khalaf, Higher-order topological insulators and superconductors protected by inversion symmetry, Phys. Rev. B **97**, 205136 (2018).

[24] P. Szumniak, D. Loss, and J. Klinovaja, Hinge modes and surface states in second-order topological three-dimensional quantum Hall systems induced by charge density modulation, Phys. Rev. B **102**, 125126 (2020).

[25] B. Xie, H. X. Wang, X. Zhang, P. Zhan, J. H. Jiang, M. Lu, and Y. Chen, Higher-order band topology, Nat. Rev. Phys. **3**, 520 (2021).

[26] A. Eckardt, Colloquium: Atomic quantum gases in periodically driven optical lattices, Rev. Mod. Phys. **89**, 011004 (2017).

[27] T. Oka and S. Kitamura, Floquet engineering of quantum materials, Annu. Rev. Condens. Matter Phys. **10**, 387 (2019).

[28] Y. Kayanuma and K. Saito, Coherent destruction of tunneling, dynamic localization, and the Landau-Zener formula, Phys. Rev. A **77**, 010101(R) (2008).

[29] T. Nag, S. Roy, A. Dutta, and D. Sen, Dynamical localization in a chain of hard core bosons under periodic driving, Phys. Rev. B **89**, 165425 (2014).

[30] T. Nag, D. Sen, and A. Dutta, Maximum group velocity in a one-dimensional model with a sinusoidally varying staggered potential, Phys. Rev. A **91**, 063607 (2015).

[31] L. D'Alessio and A. Polkovnikov, Many-body energy localization transition in periodically driven systems, Ann. Phys. **333**, 19 (2013).

[32] L. D'Alessio and M. Rigol, Long-Time Behavior of Isolated Periodically Driven Interacting Lattice Systems, Phys. Rev. X **4**, 041048 (2014).

[33] P. Ponte, A. Chandran, Z. Papić, and D. A. Abanin, Periodically driven ergodic and many-body localized quantum systems, Ann. Phys. **353**, 196 (2015).

[34] D. V. Else, B. Bauer, and C. Nayak, Floquet Time Crystals, Phys. Rev. Lett. **117**, 090402 (2016).

[35] V. Khemani, A. Lazarides, R. Moessner, and S. L. Sondhi, Phase Structure of Driven Quantum Systems, Phys. Rev. Lett. **116**, 250401 (2016).

[36] T. Nag, R.-J. Slager, T. Higuchi, and T. Oka, Dynamical synchronization transition in interacting electron systems, Phys. Rev. B **100**, 134301 (2019).

[37] T. N. Ikeda, K. Chinzei, and H. Tsunetsugu, Floquet-theoretical formulation and analysis of high-order harmonic generation in solids, Phys. Rev. A **98**, 063426 (2018).

[38] T. Oka and H. Aoki, Photovoltaic Hall effect in graphene, Phys. Rev. B **79**, 081406(R) (2009).

[39] T. Kitagawa, T. Oka, A. Brataas, L. Fu, and E. Demler, Transport properties of nonequilibrium systems under the application of light: Photoinduced quantum Hall insulators without Landau levels, Phys. Rev. B **84**, 235108 (2011).

[40] N. H. Lindner, G. Refael, and V. Galitski, Floquet topological insulator in semiconductor quantum wells, Nat. Phys. **7**, 490 (2011).

[41] M. S. Rudner, N. H. Lindner, E. Berg, and M. Levin, Anomalous Edge States and the Bulk-Edge Correspondence for Periodically Driven Two-Dimensional Systems, Phys. Rev. X **3**, 031005 (2013).

[42] T. Nag and B. Roy, Anomalous and normal dislocation modes in floquet topological insulators, Commun. Phys. **4**, 157 (2021).

[43] M. S. Rudner and N. H. Lindner, Band structure engineering and non-equilibrium dynamics in floquet topological insulators, Nat. Rev. Phys. **2**, 229 (2020).

[44] M. Thakurathi, A. A. Patel, D. Sen, and A. Dutta, Floquet generation of Majorana end modes and topological invariants, Phys. Rev. B **88**, 155133 (2013).

[45] M. Benito, A. Gómez-León, V. M. Bastidas, T. Brandes, and G. Platero, Floquet engineering of long-range p-wave superconductivity, Phys. Rev. B **90**, 205127 (2014).

[46] P. D. Sacramento, Charge and spin edge currents in two-dimensional Floquet topological superconductors, Phys. Rev. B **91**, 214518 (2015).

[47] R.-X. Zhang and S. Das Sarma, Anomalous Floquet Chiral Topological Superconductivity in a Topological Insulator Sandwich Structure, Phys. Rev. Lett. **127**, 067001 (2021).

[48] Y. H. Wang, H. Steinberg, P. Jarillo-Herrero, and N. Gedik, Observation of floquet-bloch states on the surface of a topological insulator, Science **342**, 453 (2013).

[49] Y.-G. Peng, C.-Z. Qin, D.-G. Zhao, Y.-X. Shen, X.-Y. Xu, M. Bao, H. Jia, and X.-F. Zhu, Experimental demonstration of anomalous floquet topological insulator for sound, Nat. Commun. **7**, 13368 (2016).

[50] R. Fleury, A. B. Khanikaev, and A. Alu, Floquet topological insulators for sound, Nat. Commun. **7**, 11744 (2016).

[51] M. C. Rechtsman, J. M. Zeuner, Y. Plotnik, Y. Lumer, D. Podolsky, F. Dreisow, S. Nolte, M. Segev, and A. Szameit, Photonic floquet topological insulators, Nature (London) **496**, 196 (2013).

[52] L. J. Maczewsky, J. M. Zeuner, S. Nolte, and A. Szameit, Observation of photonic anomalous floquet topological insulators, Nat. Commun. **8**, 13756 (2017).

[53] T. Nag, V. Juričić, and B. Roy, Out of equilibrium higher-order topological insulator: Floquet engineering and quench dynamics, Phys. Rev. Research **1**, 032045(R) (2019).

[54] R. W. Bomantara, L. Zhou, J. Pan, and J. Gong, Coupled-wire construction of static and Floquet second-order topological insulators, Phys. Rev. B **99**, 045441 (2019).

[55] R. Seshadri, A. Dutta, and D. Sen, Generating a second-order topological insulator with multiple corner states by periodic driving, Phys. Rev. B **100**, 115403 (2019).

[56] M. Rodriguez-Vega, A. Kumar, and B. Seradjeh, Higher-order Floquet topological phases with corner and bulk bound states, Phys. Rev. B **100**, 085138 (2019).

[57] B. Huang and W. V. Liu, Floquet Higher-Order Topological Insulators with Anomalous Dynamical Polarization, Phys. Rev. Lett. **124**, 216601 (2020).

[58] A. K. Ghosh, G. C. Paul, and A. Saha, Higher order topological insulator via periodic driving, Phys. Rev. B **101**, 235403 (2020).

[59] Y. Peng and G. Refael, Floquet Second-Order Topological Insulators from Nonsymmorphic Space-Time Symmetries, Phys. Rev. Lett. **123**, 016806 (2019).

[60] Y. Peng, Floquet higher-order topological insulators and superconductors with space-time symmetries, Phys. Rev. Research **2**, 013124 (2020).

[61] T. Nag, V. Juričić, and B. Roy, Hierarchy of higher-order Floquet topological phases in three dimensions, Phys. Rev. B **103**, 115308 (2021).

[62] R.-X. Zhang and Z.-C. Yang, Tunable fragile topology in Floquet systems, Phys. Rev. B **103**, L121115 (2021).

[63] H. Hu, B. Huang, E. Zhao, and W. V. Liu, Dynamical Singularities of Floquet Higher-Order Topological Insulators, Phys. Rev. Lett. **124**, 057001 (2020).

[64] W. Zhu, Y. D. Chong, and J. Gong, Floquet higher-order topological insulator in a periodically driven bipartite lattice, Phys. Rev. B **103**, L041402 (2021).

[65] A. K. Ghosh, T. Nag, and A. Saha, Floquet generation of a second-order topological superconductor, Phys. Rev. B **103**, 045424 (2021).

[66] A. K. Ghosh, T. Nag, and A. Saha, Floquet second order topological superconductor based on unconventional pairing, Phys. Rev. B **103**, 085413 (2021).

[67] J. Yu, R.-X. Zhang, and Z.-D. Song, Dynamical symmetry indicators for floquet crystals, Nat. Commun. **12**, 5985 (2021).

[68] D. Vu, Dynamic bulk-boundary correspondence for anomalous Floquet topology, Phys. Rev. B **105**, 064304 (2022).

[69] A. K. Ghosh, T. Nag, and A. Saha, Hierarchy of higher-order topological superconductors in three dimensions, Phys. Rev. B **104**, 134508 (2021).

[70] F. Schindler, Z. Wang, M. G. Vergniory, A. M. Cook, A. Murani, S. Sengupta, A. Y. Kasumov, R. Deblock, S. Jeon, I. Drozdov *et al.*, Higher-order topology in bismuth, Nat. Phys. **14**, 918 (2018).

[71] R. Noguchi, M. Kobayashi, Z. Jiang, K. Kuroda, T. Takahashi, Z. Xu, D. Lee, M. Hirayama, M. Ochi, T. Shirasawa *et al.*, Evidence for a higher-order topological insulator in a three-dimensional material built from van der waals stacking of bismuth-halide chains, Nat. Mater. **20**, 473 (2021).

[72] M. Serra-Garcia, V. Peri, R. Süsstrunk, O. R. Bilal, T. Larsen, L. G. Villanueva, and S. D. Huber, Observation of a phononic quadrupole topological insulator, Nature (London) **555**, 342 (2018).

[73] H. Xue, Y. Yang, F. Gao, Y. Chong, and B. Zhang, Acoustic higher-order topological insulator on a kagome lattice, Nat. Mater. **18**, 108 (2019).

[74] C. W. Peterson, W. A. Benalcazar, T. L. Hughes, and G. Bahl, A quantized microwave quadrupole insulator with topologically protected corner states, Nature (London) **555**, 346 (2018).

[75] S. Mittal, V. V. Orre, G. Zhu, M. A. Gorlach, A. Poddubny, and M. Hafezi, Photonic quadrupole topological phases, Nat. Photon. **13**, 692 (2019).

[76] S. Imhof, C. Berger, F. Bayer, J. Brehm, L. W. Molenkamp, T. Kiessling, F. Schindler, C. H. Lee, M. Greiter, T. Neupert *et al.*, Topolectrical-circuit realization of topological corner modes, Nat. Phys. **14**, 925 (2018).

[77] R. Jackiw and C. Rebbi, Solitons with fermion number ½, Phys. Rev. D **13**, 3398 (1976).

[78] P. M. Perez-Piskunow, G. Usaj, C. A. Balseiro, and L. E. F. F. Torres, Floquet chiral edge states in graphene, Phys. Rev. B **89**, 121401(R) (2014).

[79] G. Usaj, P. M. Perez-Piskunow, L. E. F. Foa Torres, and C. A. Balseiro, Irradiated graphene as a tunable Floquet topological insulator, Phys. Rev. B **90**, 115423 (2014).

[80] A. K. Ghosh, T. Nag, and A. Saha, Dynamical construction of quadrupolar and octupolar topological superconductors, arXiv:2201.07578.

[81] B. Kang, K. Shiozaki, and G. Y. Cho, Many-body order parameters for multipoles in solids, Phys. Rev. B **100**, 245134 (2019).

[82] T. Mikami, S. Kitamura, K. Yasuda, N. Tsuji, T. Oka, and H. Aoki, Brillouin-Wigner theory for high-frequency expansion in periodically driven systems: Application to Floquet topological insulators, Phys. Rev. B **93**, 144307 (2016).

[83] B. Roy, Higher-order topological superconductors in $\mathcal{P}$-, $\mathcal{T}$-odd quadrupolar Dirac materials, Phys. Rev. B **101**, 220506(R) (2020).

[84] P. Mohan, R. Saxena, A. Kundu, and S. Rao, Brillouin-Wigner theory for Floquet topological phase transitions in spin-orbit-coupled materials, Phys. Rev. B **94**, 235419 (2016).

[85] A. Kundu, H. A. Fertig, and B. Seradjeh, Floquet-Engineered Valleytronics in Dirac Systems, Phys. Rev. Lett. **116**, 016802 (2016).

[86] S. Chaudhary, A. Haim, Y. Peng, and G. Refael, Phonon-induced Floquet topological phases protected by space-time symmetries, Phys. Rev. Research **2**, 043431 (2020).

[87] K. Plekhanov, M. Thakurathi, D. Loss, and J. Klinovaja, Floquet second-order topological superconductor driven via ferromagnetic resonance, Phys. Rev. Research **1**, 032013(R) (2019).

[88] R. Roy and F. Harper, Periodic Table for Floquet topological insulators, Phys. Rev. B **96**, 155118 (2017).

[89] H. Araki, T. Mizoguchi, and Y. Hatsugai, Phase diagram of a disordered higher-order topological insulator: A machine learning study, Phys. Rev. B **99**, 085406 (2019).

[90] Y.-B. Yang, K. Li, L.-M. Duan, and Y. Xu, Higher-order topological Anderson insulators, Phys. Rev. B **103**, 085408 (2021).

[91] J.-H. Wang, Y.-B. Yang, N. Dai, and Y. Xu, Structural-Disorder-Induced Second-Order Topological Insulators in Three Dimensions, Phys. Rev. Lett. **126**, 206404 (2021).

[92] Y.-S. Hu, Y.-R. Ding, J. Zhang, Z.-Q. Zhang, and C.-Z. Chen, Disorder and phase diagrams of higher-order topological insulators, Phys. Rev. B **104**, 094201 (2021).

[93] P. Titum, E. Berg, M. S. Rudner, G. Refael, and N. H. Lindner, Anomalous Floquet-Anderson Insulator as a Nonadiabatic Quantized Charge Pump, Phys. Rev. X **6**, 021013 (2016).

[94] E. A. Rodríguez-Mena and L. E. F. Foa Torres, Topological signatures in quantum transport in anomalous Floquet-Anderson insulators, Phys. Rev. B **100**, 195429 (2019).

[95] J. Song, H. Liu, H. Jiang, Q.-F. Sun, and X. C. Xie, Dependence of topological Anderson insulator on the type of disorder, Phys. Rev. B **85**, 195125 (2012).

[96] R. Modak and T. Nag, Many-body dynamics in long-range hopping models in the presence of correlated and uncorrelated disorder, Phys. Rev. Research **2**, 012074(R) (2020).

[97] X. Ni, M. Weiner, A. Alu, and A. B. Khanikaev, Observation of higher-order topological acoustic states protected by generalized chiral symmetry, Nat. Mater. **18**, 113 (2019).

[98] X. Zhang, B.-Y. Xie, H.-F. Wang, X. Xu, Y. Tian, J.-H. Jiang, M.-H. Lu, and Y.-F. Chen, Dimensional hierarchy of higher-order topology in three-dimensional sonic crystals, Nat. Commun. **10**, 5331 (2019).

[99] W. Zhu, H. Xue, J. Gong, Y. Chong, and B. Zhang, Time-periodic corner states from floquet higher-order topology, Nat. Commun. **13**, 11 (2022).